



# Influence of Shielding Gas on the Microstructure and Mechanical Properties of Duplex Stainless Steel in Wire Arc Additive Manufacturing

Elina Akbarzadeh<sup>1</sup> · Koray Yurtışık<sup>2</sup> · C. Hakan Gür<sup>2,3</sup> · Tohid Saeid<sup>1</sup> · Reza Tavangar<sup>1</sup>

Received: 7 November 2023 / Accepted: 29 December 2023 / Published online: 10 February 2024  
© The Author(s) under exclusive licence to The Korean Institute of Metals and Materials 2024

## Abstract

This study investigates the influence of the shielding gas composition on the microstructural and mechanical properties of wire arc additive manufactured duplex stainless steel. The choice of shielding gas influences the quality and performance of these steels in various industries. Three shielding gases, namely Ar, Ar + 2wt%O<sub>2</sub> (Ar–O), and Ar + 2wt%N<sub>2</sub> (Ar–N) were used for the deposition of walls with 2209 duplex stainless steel wire. Extensive microstructural analysis and mechanical property evaluations were performed. Based on microscopic observations, the walls produced under different gases exhibited varying inclusion levels, primarily composed of silicon-rich oxide inclusions, with the Ar–O sample exhibiting the highest inclusion concentration at 1.5 vol%. Moreover, the microstructure of all samples consisted of ferrite and austenite phases with different austenite morphologies, with intergranular austenite dominating in the Ar–O sample. In three samples, different degrees of preferred orientation were found in both the ferrite and austenite phases. In this regard, the Ar and Ar–O samples had the strongest and weakest texture, respectively, owing to the influence of inclusions on the formation of a random texture. The microhardness mapping revealed the highest hardness of 250 HV in the Ar–N sample and the lowest hardness of 220 HV in the Ar–O sample. Nitrogen's strengthening effect on austenite in the Ar–N sample and the higher austenite content in the Ar–O sample were believed to be responsible for these variations. Nanohardness indentations confirmed the lower hardness of austenite compared to ferrite, corroborating the overall lower hardness observed in the Ar–O sample. The Ar–N sample exhibited the highest tensile strength and yield strength of 826 and 539 MPa, respectively in the horizontal direction, which is consistent with the observed hardness results. On the other hand, the Ar sample exhibited the highest elongation of all samples at 39%, which is consistent with its lower inclusion content.

**Keywords** Wire arc additive manufacturing (WAAM) · Duplex stainless steel (DSS) · Shielding gas · Microstructure · Mechanical properties · Inclusions

## 1 Introduction

Duplex stainless steels (DSSs) are widely used in various industries, including food, medical, automotive, oil and gas, chemical, energy, and aerospace owing to their remarkable combination of excellent corrosion resistance and exceptional mechanical strength [1, 2]. Conventional manufacturing methods, such as casting, forging, hot forming, and welding, have traditionally been employed for DSS production [3]. However, recent technological advancements have brought about the emergence of innovative additive manufacturing (AM) techniques capable of directly fabricating DSS components from digital models [4–9]. One particular AM method that has gained prominence is the wire arc additive manufacturing (WAAM) [10]. This process relies

✉ C. Hakan Gür  
chgur@metu.edu.tr

✉ Tohid Saeid  
saeid@sut.ac.ir

<sup>1</sup> Faculty of Materials Engineering, Sahand University of Technology, Tabriz 51335-1996, Iran

<sup>2</sup> Welding Technology and Nondestructive Testing Research/Application Center, Middle East Technical University, 06800 Ankara, Turkey

<sup>3</sup> Department of Metallurgical and Materials Engineering, Middle East Technical University, 06800 Ankara, Turkey

on welding principles, where a welding wire is melted by an electric arc between the wire and the substrate. A welding robot then methodically deposits sequential layers of molten metal, gradually constructing the desired 3D structure [11–14]. WAAM offers several compelling advantages, including cost-effectiveness in producing large and intricate industrial components, and the efficient utilization of raw materials [15, 16]. This production method has opened up new possibilities for manufacturing complex geometries and tailoring properties precisely, enabling the creation of innovative solutions for challenging applications across various industries. Among the critical parameters that influence the success of WAAM in DSS fabrication is the composition of shielding gas. The shielding gas directly impacts the chemical composition of the molten pool and, consequently, the desired 1:1 ratio of austenite ( $\gamma$ ) and ferrite ( $\delta$ ) phases in the matrix of the produced DSS. This ratio directly influences the final mechanical properties of the as-manufactured component.

Most research on shielding gases for DSSs production has focused on welding processes rather than WAAM. In welding DSSs, the most commonly used shielding gases include argon, helium, or mixtures of argon with gases like carbon dioxide, oxygen, nitrogen, or hydrogen [17–19].

A common combination involves mixing argon with a small amount of oxidizing gases such as oxygen or carbon dioxide [20, 21]. It is well-documented that adding oxygen to the shielding gas enhances arc stability, reduces welding sparks, and enables more even welding with lower heat input [22–24]. Oxygen also plays a critical role in preserving nitrogen levels by increasing its solubility within the weld metal [25, 26]. A study by Zou et al. [27], noted that oxygen within the arc plasma further diminishes nitrogen loss by forming an oxide layer on the surface of the weld pool, preventing its escape. Controlling nitrogen content in DSSs is essential, as it promotes austenite formation and facilitates a 1:1  $\gamma/\delta$  balance [28, 29]. However, oxygen present in the shielding gas can also result in the formation of oxide inclusions and alter the depth-to-width ratio in welding DSSs [27].

In welding DSSs, it is also common to use argon gas mixtures with an optimal nitrogen content [17, 30–32]. Nitrogen plays a crucial role in the development of DSSs by acting as an austenite stabilizer, improving their mechanical properties and corrosion resistance [33]. However, reports have indicated nitrogen loss from the weld pool during the welding process. Nitrogen is lost from the base metal by entering the weld pool and then evaporating due to the heat generated by the arc [34]. The extent of the loss is determined by the difference between the rate of desorption and adsorption from/into the weld pool [17]. The loss of nitrogen from both the weld pool and the heat-affected zone (HAZ) can lead to reduced toughness, decreased resistance

to pitting corrosion, and increased vulnerability to hydrogen embrittlement due to excessive ferrite. Therefore, the primary purpose of introducing nitrogen into the shielding gas is to compensate for this nitrogen loss during welding [35, 36]. According to Zhang et al. [37] an optimal nitrogen content of 2% can effectively prevent nitrogen losses during the welding process.

While many investigations have examined the impact of shielding gases on the welding of DSSs, their significance is often overlooked in the existing research on WAAM. For example, in a study on WAAM of DSS, Hosseini et al. [38] employed pure Ar as a shielding gas. They theorized that the diminished austenite content observed at higher heat inputs might be attributed to nitrogen loss, emphasizing the need for further studies involving nitrogen addition to the shielding gas. Cederberg et al. [39] also highlighted nitrogen loss as a critical challenge in WAAM of DSSs.

Despite the established use of nitrogen and oxygen with argon as a shielding gas for DSS welds, the existing literature on the impact of shielding gas on WAAM of DSSs is fragmented and lacks standardized experimental conditions. No study has systematically investigated these effects while maintaining parameters constant. Therefore, the primary objective of this research is to address this gap by meticulously controlling influential variables such as heat input and interlayer temperature in order to isolate the impact of shielding gas. The novelty of this study lies in its comprehensive examination of how the shielding gases Ar, Ar + 2% O<sub>2</sub>, and Ar + 2% N<sub>2</sub>, which are commonly employed for welding DSSs, affect their microstructure and mechanical properties when produced using WAAM under identical fabrication parameters. This research enhances our understanding of the WAAM process for DSS fabrication. It offers practical insights for industries using these materials, guiding better choices in shielding gases for different applications. This affects the quality, performance, and cost-effectiveness of DSS components across various industries.

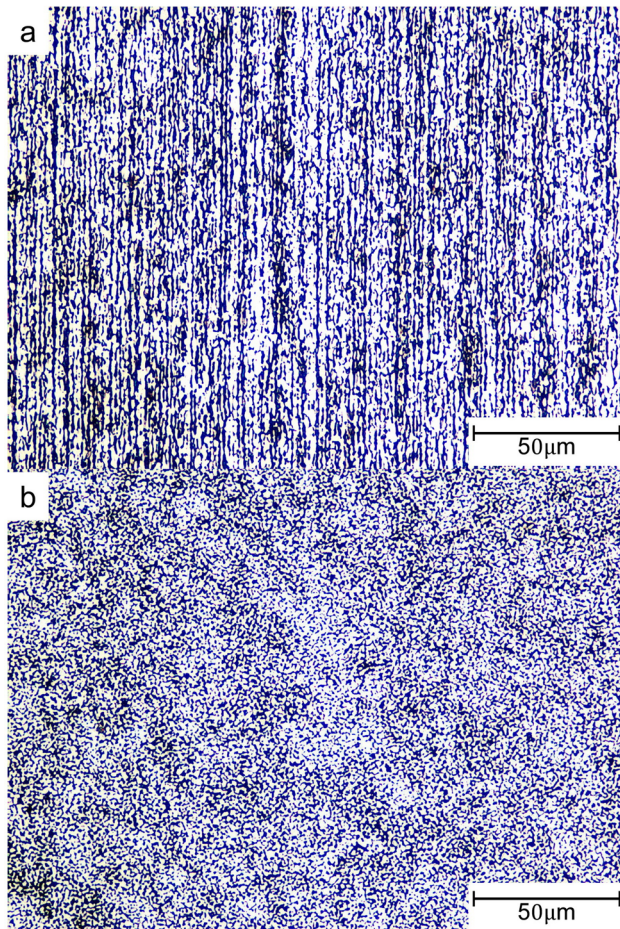
## 2 Experimental Procedure

### 2.1 Experimental Setup and Material

An ABB IRC5 M2004 robot paired with a Fronius TransPuls Synergic 3200 power source was used for WAAM process using a single-bead multi-layer deposition strategy. The wire used was 2209 DSS (Thermanit-Bohler) with a diameter of 1.2 mm. The mechanical properties of the wire are listed in Table 1. Figure 1 shows the optical images of the wire from both sections, which have an austenite/ferrite ratio of 55/45. Three shielding gases; Ar, Ar + 2% O<sub>2</sub>, and Ar + 2% N<sub>2</sub> (in wt%), all at a constant flow rate of 20 L/min for each shielding gas, were

**Table 1** Hardness, yield strength (YS), ultimate tensile strength (UTS), elongation (El) of the 2209 DSS wire

	Hardness (HV)	YS (MPa)	UTS (MPa)	El (%)
2209 DSS	355 ± 5 HV	650	720	25

**Fig. 1** The optical micrograph of 2209 DSS wire from **a** longitudinal and **b** cross sections

used to produce walls with 40 layers in height. In order to investigate the influence of shielding gases in Isolation, all walls were produced with carefully selected welding parameters to ensure a uniform heat input of 0.56 kJ/mm. The walls were built on a substrate made of 2205 DSS with dimensions of 300 × 300 × 25 mm<sup>3</sup>. The contact tip to work distance (CTWD) was set to 15 mm, and the interpass temperature was maintained at 230 ± 5 °C. A schematic representation of the WAAM process is illustrated in Fig. 2a. The produced walls using three different shielding gases are shown in Fig. 2b.

To facilitate clear identification of the walls and samples produced by using different shielding gases, this article

consistently uses the following abbreviations: Ar, Ar–O, and Ar–N, respectively.

After fabrication, the walls were separated from the substrate using an electrical discharge machine (EDM) and samples were prepared for tensile testing, X-ray diffraction analysis (XRD), optical microscopy (OM), field emission scanning electron microscopy (FESEM) and electron backscatter diffraction (EBSD) using the configuration shown in Fig. 3. The chemical compositions of the feed wire and the fabricated walls taken from the centre are listed in Table 2.

## 2.2 Microstructural Characterizations

The standard metallographic procedure included several steps: grinding with silicon carbide papers with grit sizes from 60 to 5000 on an automatic grinding machine, followed by polishing with 3 and 1 μm diamond pastes. The EBSD samples were further polished with colloidal silica solution for at least 4 h on an automatic polishing machine. For optical microscopy, the samples were etched with Beraha II solution, and for FESEM studies, they were etched with oxalic acid. Optical microscopy was performed using a Nikon ECLIPS E200 instrument, while electron microscopy, elemental analysis and mapping of the samples were performed with a TESCAN MIRA3 FESEM instrument with energy dispersive spectroscopy (EDS). EBSD analysis was carried out using the QUANTA 400F FESEM system to investigate microstructural details of the samples. The oxygen and nitrogen concentrations in the samples were analyzed using the LECO ONH 836 analyzer. A Bruker D8 Advance XRD instrument was used to determine the γ volume fraction. The diffraction patterns were recorded with Cu Kα radiation at a voltage of 40 kV and a current of 40 mA. Scanning was performed in the 2θ range of 30°–110° with a step size of 0.02° and a step time of 3 s. Peaks corresponding to planes (111), (200), (220), (311) and (222) of γ and planes (110), (200), (211) and (220) of δ were selected to minimize errors due to preferential phase orientation. The areas under these peaks were measured using HighScore plus software to minimize errors due to background radiation. The γ volume fraction was determined from the integrated areas under the γ and δ peaks [40].

## 2.3 Mechanical Testing

Microhardness measurements were performed using an HMV Shimadzu device with a force of 9.8 N, mapping measurements were performed in the x and y directions with a point spacing of 1.27 mm, and nanoindentation tests were performed with a CSM-NHT-MB-01 device with a Berkovich indenter with a force of 300 mN. The nanoindentation device was equipped with a camera to ensure precise indentations on the intended phases. Longitudinal

**Fig. 2** Apple **a** Schematic representation of wire arc additive manufacturing process **b** as-built images illustrating the walls constructed using various shielding gas compositions

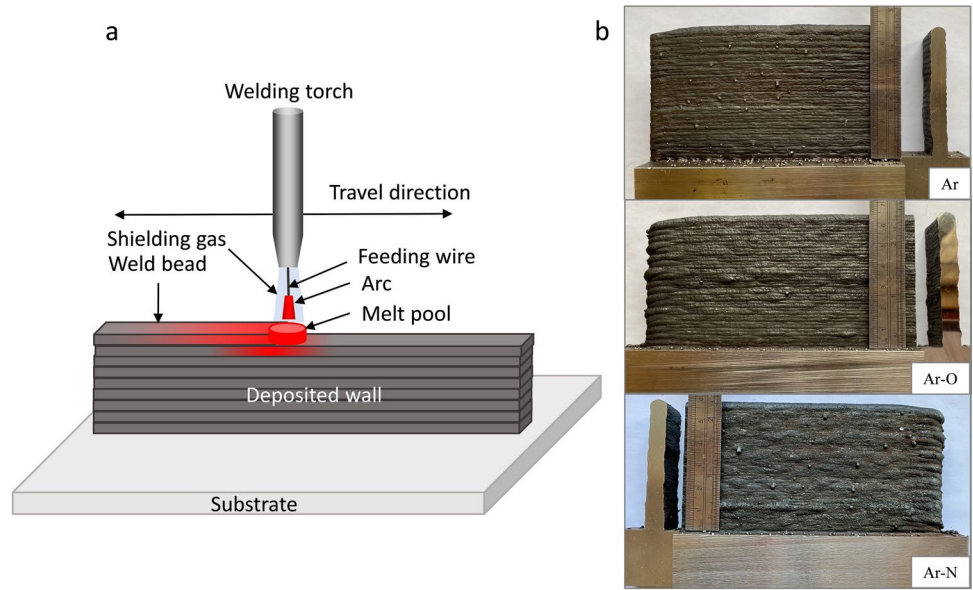


**Fig. 3** The configurations of test specimens prepared from the produced walls

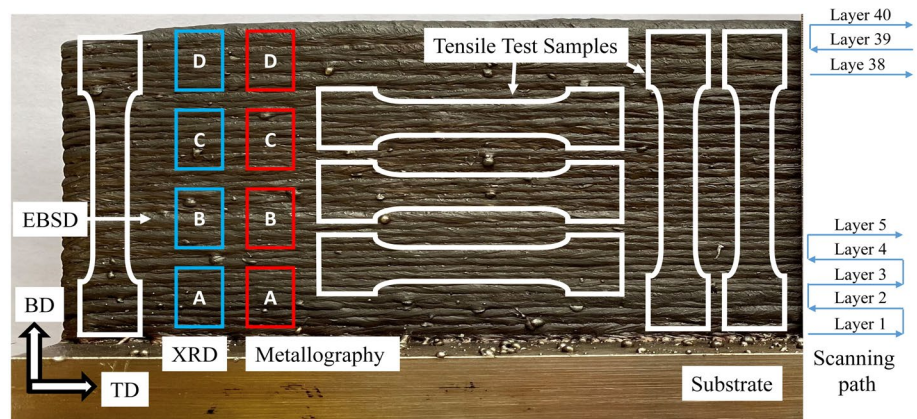


**Table 2** Chemical composition of 2209 DSS wire and deposited walls using Ar, Ar–O, and Ar–N shielding gases (wt%)

	C	Si	Mn	P	S	Cr	Mo	Ni	Cu	N*	O**
2209 DSS	0.02	0.40	1.40	0.019	0.001	23.10	3.2	8.6	<0.1	0.180	-
Ar Wall	0.031	0.34	1.38	0.015	0.009	23.02	3.86	8.64	0.046	0.150	0.037
Ar–O Wall	0.029	0.33	1.34	0.015	0.015	23.01	3.64	8.86	0.047	0.174	0.091
Ar–N Wall	0.024	0.34	1.39	0.008	0.007	23.04	3.47	8.65	0.043	0.225	0.047

\*Standard deviation = ±0.0004, Expanded uncertainty = ±0.0008 (k=2, @95%confidence)

\*\*Standard deviation = ±0.0004, Expanded uncertainty = ±0.0009 (k=2, @95%confidence)

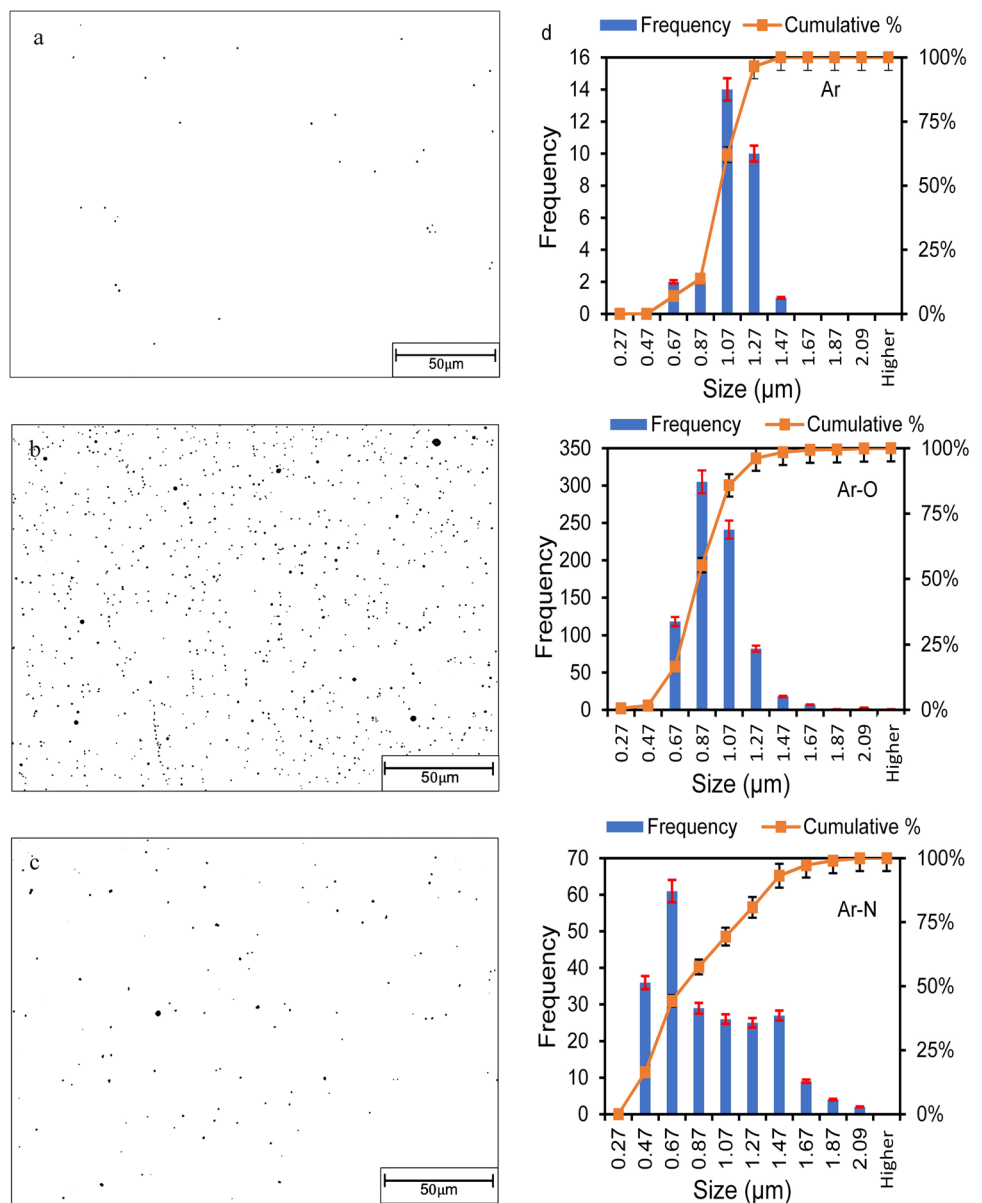
and transvers tensile tests were performed on specimens prepared according to the JIS Z 2201 standard (Fig. 3) with a thickness of 3 mm and a gauge length of one inch. The tensile tests were performed using a Besmak BMT-E testing machine at room temperature and a crosshead speed of 0.5 mm/min.

### 3 Results and Discussions

#### 3.1 Microstructural Observations

Figure 4a–c show microscopic images of polished samples

**Fig. 4** Optical micrographs of samples produced using **a** Ar, **b** Ar–O and **c** Ar–N shielding gases showing the inclusions present in the matrix. **d** Size distribution of the inclusions for micrographs a, b and c respectively



of three different walls produced with Ar, Ar–O and Ar–N shielding gases, respectively. These micrographs show the presence of small inclusions, with the highest concentration observed in the Ar–O sample and the lowest in the Ar sample. Using ImageJ software, the volume fraction of inclusions was determined to be 0.06% for the Ar sample, 1.5% for the Ar–O sample and 0.24% for the Ar–N sample. The quantitative size distribution of the inclusions for all three samples is shown in Fig. 4d revealing that the majority of the inclusions in all samples have a size in the sub-micron range. No clusters or accumulations of inclusions can be seen in the microscopic images. Inclusions were also found on the fracture surfaces of the tensile samples.

Oxide-rich inclusions usually rise and form a slag at the top of the melt due to their lower density. However, smaller

inclusions may be trapped between the dendrite arms as they rise more slowly to the top of the melt. As the number of deposited layers increases, the thickness of the slag layer also increases, increasing the likelihood of entrapment of remelted slag layers [41].

When Ar–N gas was used as the shielding gas, the arc exhibited lower stability compared to pure Ar, which could explain the higher inclusion content in the corresponding samples. Lower arc stability was also observed in previous studies with similar shielding gases [42, 43]. In the case of the Ar–O sample, despite the high stability of the arc, the presence of oxygen in the shielding gas during the manufacturing process could have led to the formation of oxide inclusions that were trapped during the remelting and solidification process. As the WAAM process is more susceptible

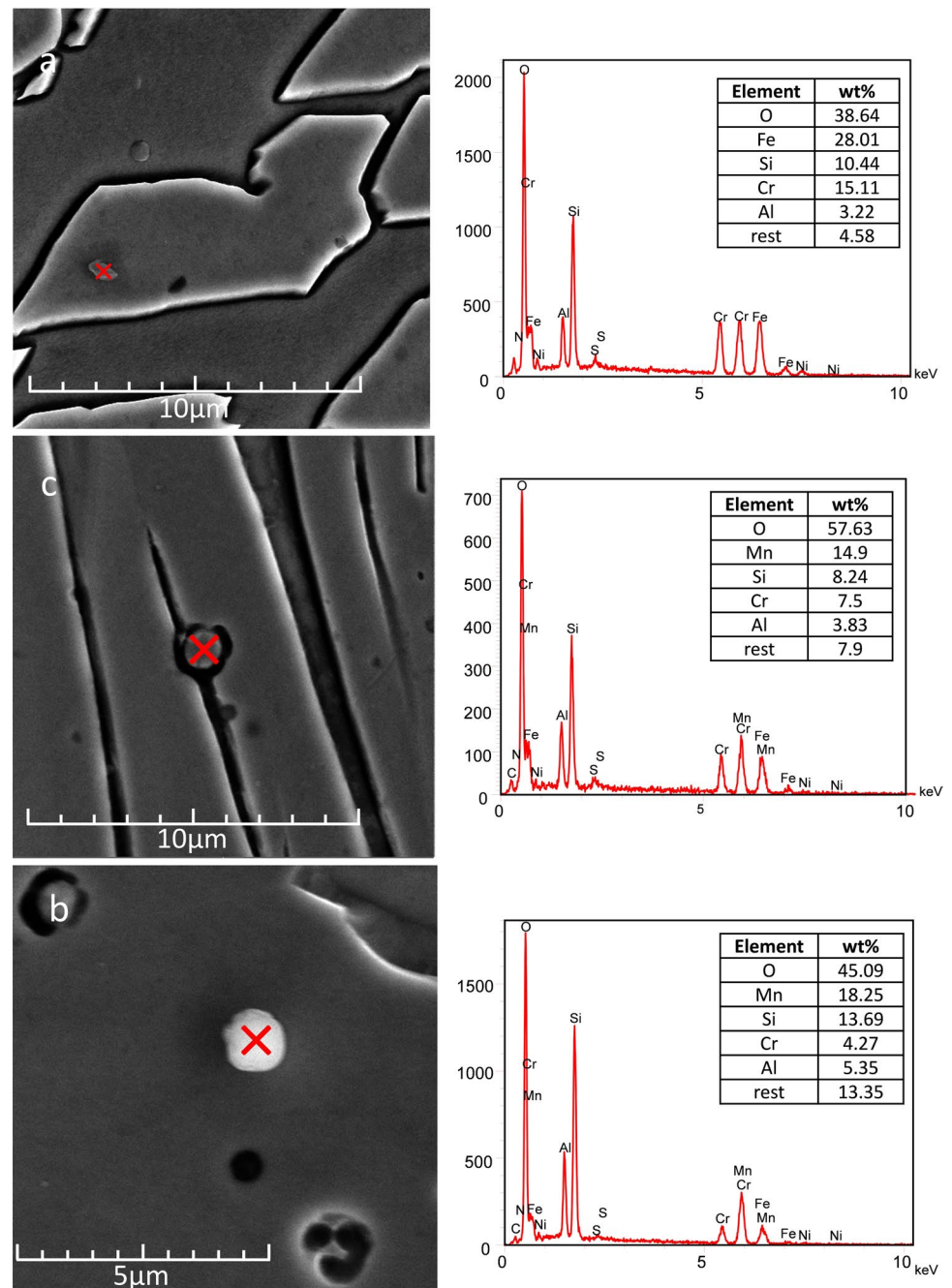
to the formation of inclusions than conventional single-pass welding processes, the choice of shielding gas is of greater importance with WAAM than with normal single-pass welding processes.

Multiple EDS analyses of inclusions from all samples revealed that they consist mainly of silicon-rich oxides, although some manganese-rich oxides were also observed. No significant preference was observed in the distribution of the different types of inclusions within each sample. Examples of EDS analyses of a silicon-rich oxide inclusion from the Ar and Ar–O samples and a manganese-rich

oxide inclusion from the Ar–N sample are shown in Fig. 5. Accordingly, the Ar–O sample with the highest content of inclusions was selected for EDS mapping from an area with multiple inclusions, which is shown in Fig. 6. It can be seen from the micrograph that all inclusions in the micrograph are silicon-rich oxides.

Figure 7a–c show micrographs of Ar, Ar–O, and Ar–N samples respectively, with the built direction (BD) indicated in the micrographs. Red dashed lines were drawn next to the interfaces to indicate their location and emphasize the columnar structure. Yellow lines were also added

**Fig. 5** Micrographs of inclusions and corresponding EDS analysis for **a** Ar, **b** Ar–O and **c** Ar–N samples



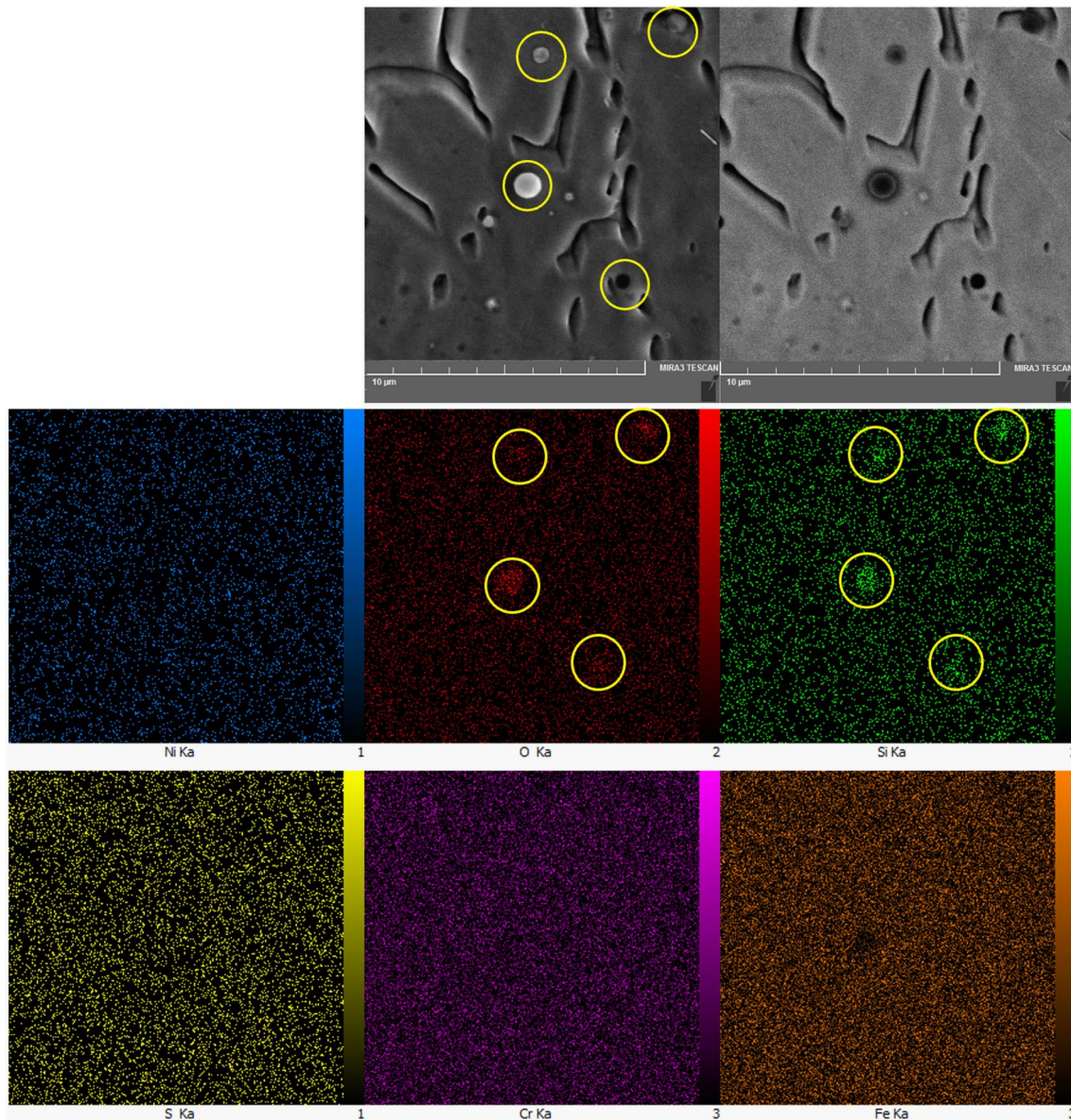


**Fig. 6** EDS elemental mapping analysis of the Ar–O sample, highlighting oxygen and silicon-rich inclusions

to distinguish each new layer boundary from the previous one.

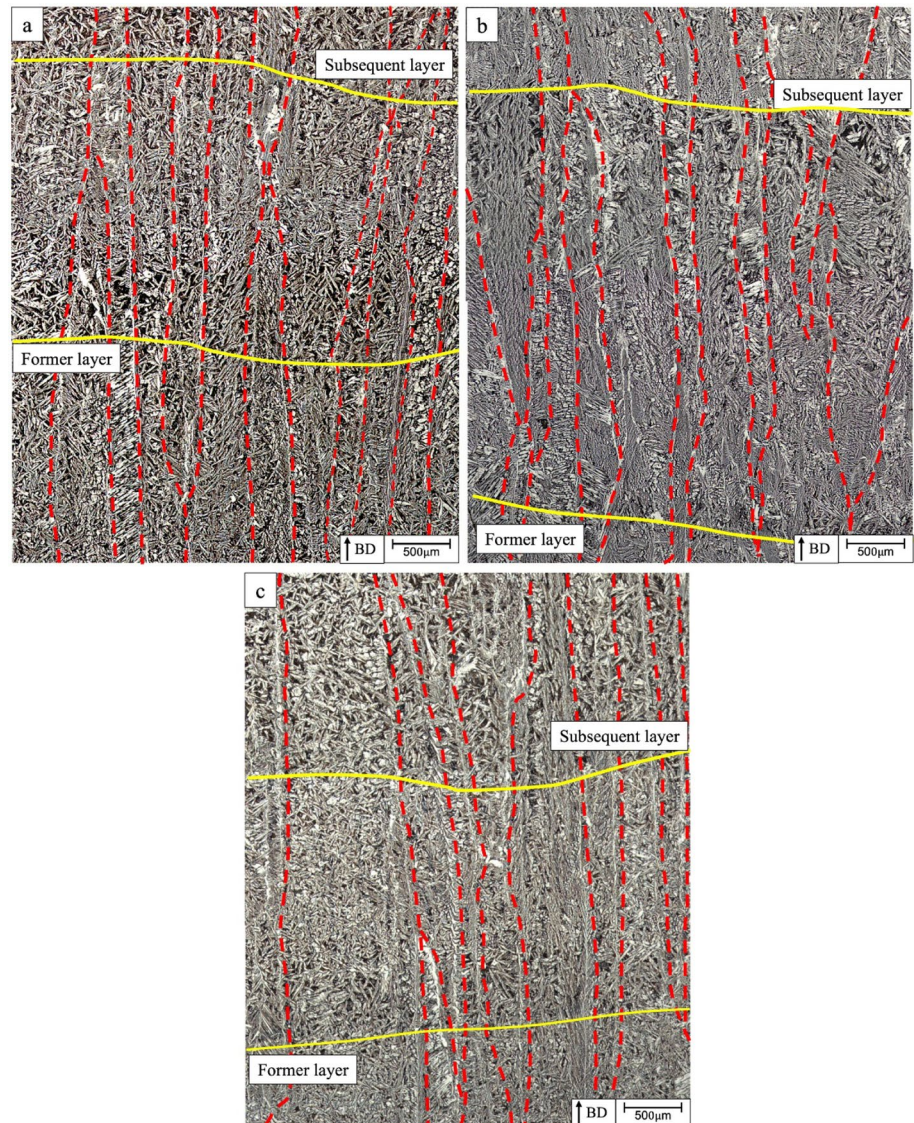
It is evident from the micrographs that the columnar morphology extends over several deposited layers. This indicates epitaxial growth, a common observation in welds with similar compositions of both the base metal and the melt. The interfaces are oriented in the build-up direction due to heat transfer towards the substrate, opposite to the BD. This leads to directional solidification during the manufacturing process [44].

Figure 8a–c show higher magnification micrographs of samples produced using Ar, Ar–O and Ar–N shielding gases and provide detailed insights into the phases and their

respective morphologies. In these images, the austenite is white and the ferrite is black due to the application of the Beraha etchant. The volume fraction of the austenite exceeds that of the ferrite in all images. These micrographs reveal a variety of austenite morphologies, including grain boundary austenite (GBA), Widmanstatten austenite (WA), intragranular austenite (IGA) and secondary austenite (SE). However, careful examination of several images reveals that IGA is the predominant austenite morphology in the Ar–O sample, as can be seen in Fig. 9a, at lower magnification micrograph of the Ar–O sample.

During the WAAM process, the previously deposited layers undergo heating and cooling cycles while new layers

**Fig. 7** Optical micrographs of samples produced using **a** Ar, **b** Ar–O and **c** Ar–N shielding gases, revealing the columnar structure and deposited layers. Etching reagent: Beraha II



are added. The austenite phase in these layers decomposes depending on the extent of the temperature increase. It can either completely transform into ferrite or partially dissolve and form a metastable ferrite phase. This formed ferrite tends to transform into austenite during subsequent cooling. GBA forms in the temperature range of 1350–800 °C, followed by the formation of WA at lower temperatures, while IGA requires a greater driving force and forms at lower temperatures [45]. In this study, the cooling rate remained the same for all samples produced with different shielding gases at identical wall positions by selecting similar heat inputs and interlayer temperatures. However, in addition to the cooling rate, the inclusion content can also influence the formation of austenite. The dominance of IGA morphology in the Ar–O sample is attributed to a larger volume of inclusions in the samples. The inclusion interfaces provide suitable sites for austenite nucleation.

Figure 9b shows a higher magnification micrograph of the region marked in Fig. 9a, which reveals the finer morphology of SA compared to IGA. This finer morphology of SA is attributed to its formation at lower temperatures [38]. While it increases toughness, it has been reported that this austenite morphology can potentially affect the corrosion resistance of DSS [46]. SA morphology was mainly observed in the Ar–O and Ar–N samples, with the Ar–N sample having a lower volume. Previous studies have indicated that the presence of precipitates may influence the formation of SA [47].

In Fig. 10, higher magnification FESEM micrographs of SA region within the Ar–O and Ar–N samples are shown. Submicron inclusions can be seen in the micrographs which are marked with small circles for easier identification. Their number is higher in Ar–O sample and it appears that there is a correlation between the formation of SA and the presence of these fine inclusions.



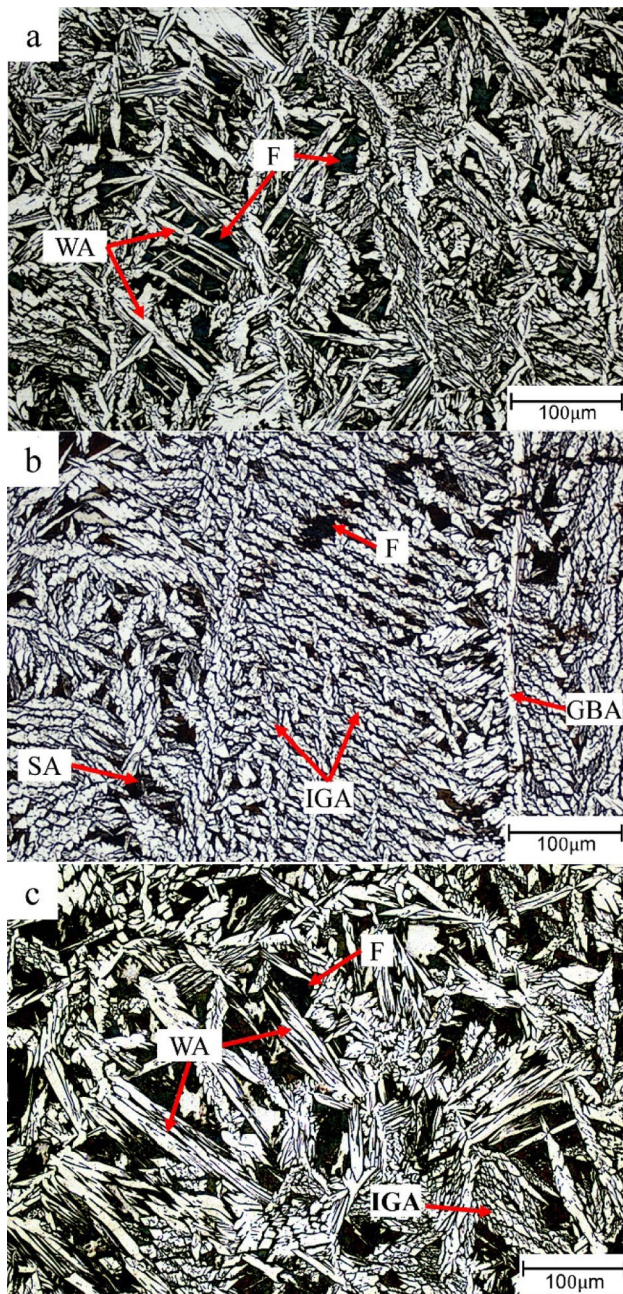


**Fig. 8** Optical micrographs of samples produced using **a** Ar, **b** Ar–O, and **c** Ar–N shielding gases showing various austenite morphologies and the ferrite phase. Abbreviations used on the micrographs: GBA: Grain boundary austenite; IGA: Intragranular austenite; WA: Widmanstätten austenite; SE: Secondary austenite; F: Ferrite

### 3.2 XRD Analysis

Optical microscopy showed a relatively higher  $\gamma$  content compared to the  $\delta$  content in the samples. This observation is consistent with findings in the literature indicating that despite efforts to control the idle time and interlayer temperature for each layer of the deposited walls, the  $\gamma$  content

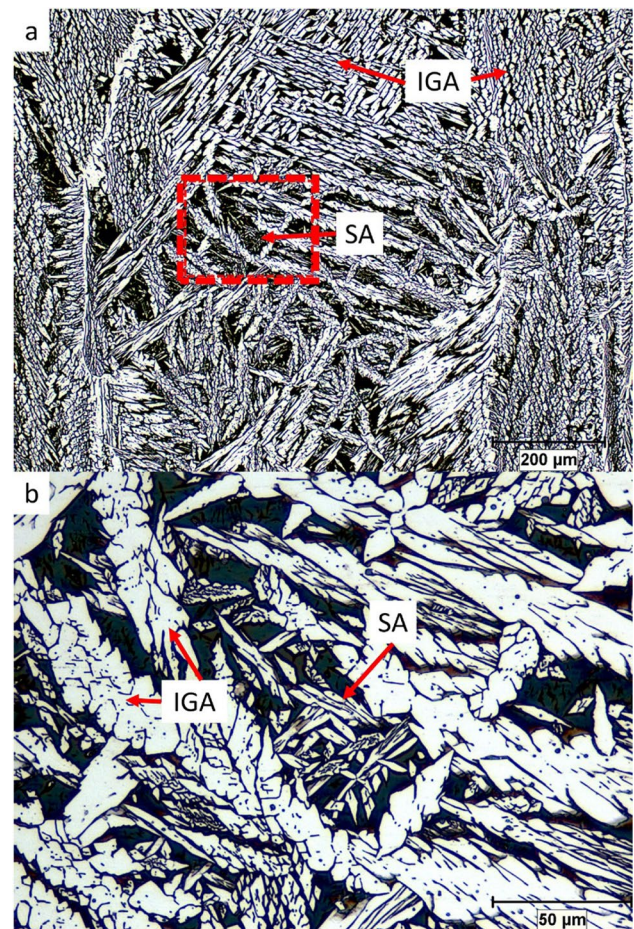


**Fig. 9** Optical micrographs of samples produced using Ar–O showing secondary austenite (SA) at low **a** and high **b** magnifications

in WAAM parts exceeds the 1:1 ratio typically observed in DSS [48–50]. The heating and cooling cycles in WAAM maintain higher temperatures and favor the formation of  $\gamma$ , a diffusion-controlled process [51].

For a quantitative analysis, the  $\delta$  and  $\gamma$  contents of the manufactured walls were determined by XRD analysis on samples taken from the bottom to the top of the walls (sample A–D), as illustrated in Fig. 3. The XRD patterns for all samples are presented in Fig. 11 and the corresponding  $\gamma$  volume fractions are reported in Fig. 12. The changes in  $\gamma$  volume fraction from sample A to D exhibit a consistent trend across the three walls. Sample A displays the lowest fraction, followed by an increase in samples B and C and a subsequent decrease in sample D, which is from the top of the walls. These results confirm the deviation from the expected  $\gamma$  to  $\delta$  ratio of 1:1 in DSS observed in the microscopic images.

During the manufacturing process, the cooling rates gradually decrease from position A–C. This decrease is due to heat accumulation in the substrate, which also serves as

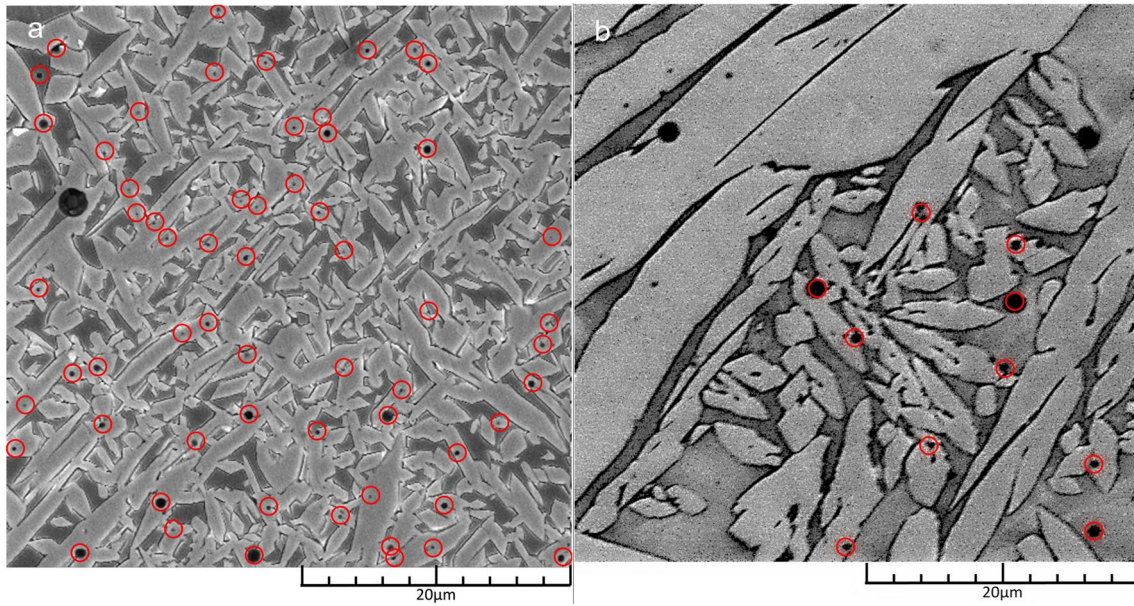


**Fig. 10** FESEM micrographs of the **a** Ar–O and **b** Ar–N samples showing secondary austenite areas. The inclusions are marked with red circles

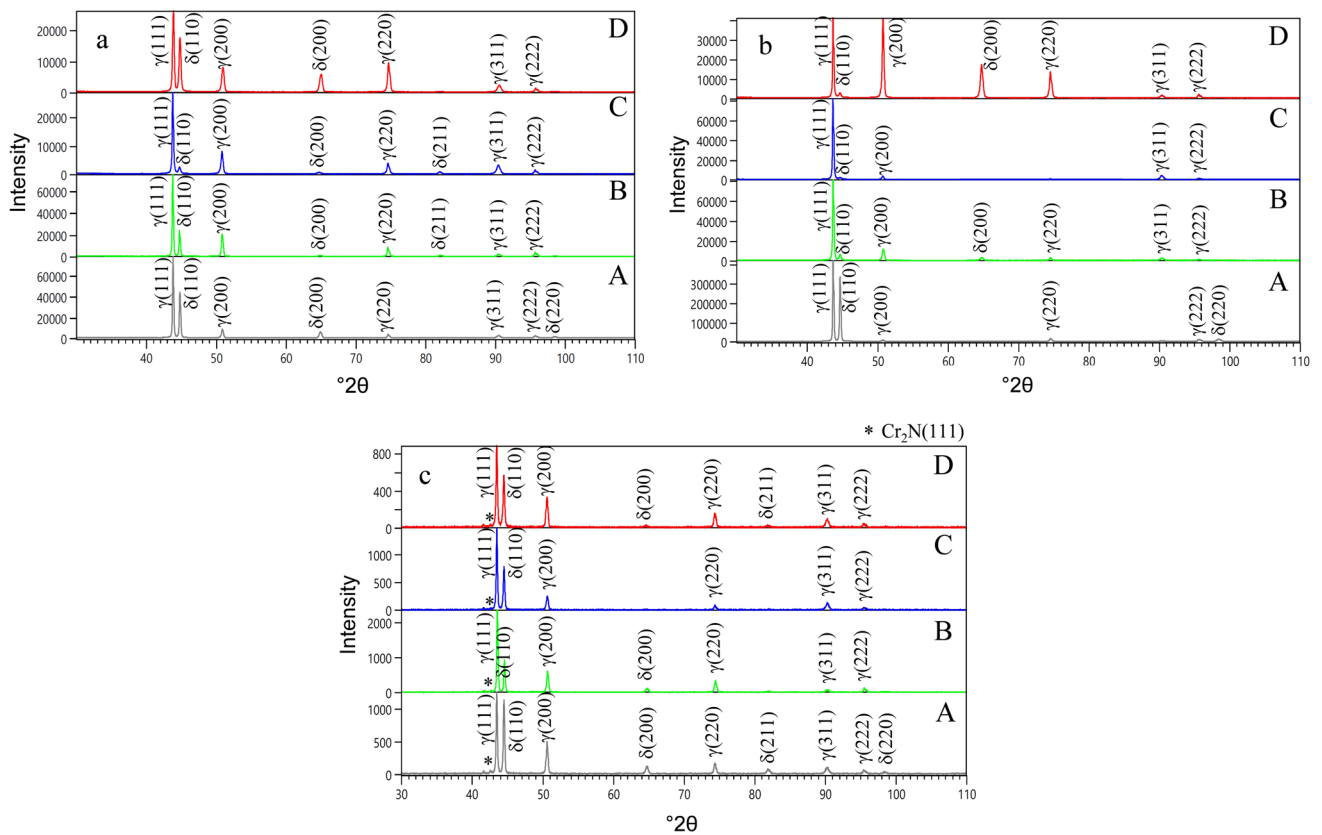


**Fig. 11** XRD patterns of the samples taken from bottom to the top (A–D) of walls produced using **a** Ar, **b** Ar–O, and **c** Ar–N shielding gases

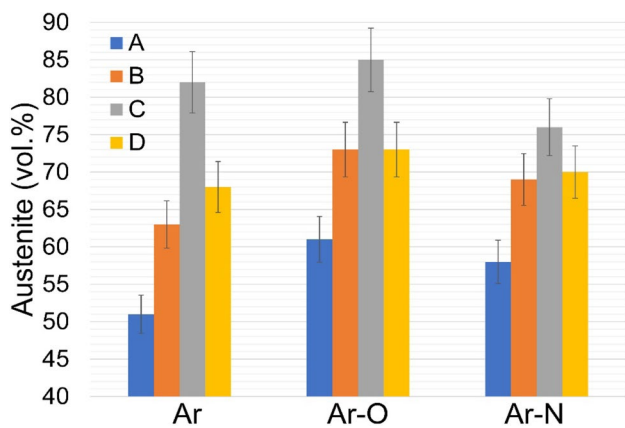


**Fig. 12** Austenite volume percent determined using XRD for walls produced using Ar, Ar-O, and Ar-N from the bottom to top of the wall (A–C samples)

a heat sink for the walls. However, sample D cools faster than sample C because heat is dissipated not only from the substrate (bottom) but also from the top. As already mentioned, the formation of  $\gamma$  is a diffusion-controlled process that is significantly influenced by the cooling rate, and these observed variations can be logically explained.

Furthermore, the results show that even with identical fabrication parameters, such as heat input (controlled by

wire feed speed, current intensity and travel speed), the Ar-O sample has a higher  $\gamma$  volume fraction at similar positions within the sample compared to the other two samples. This difference is attributed to the increased driving force for  $\gamma$  formation resulting from the presence of inclusions. In contrast, the Ar-N sample had a lower  $\gamma$  content than the Ar-O sample despite the stabilizing effect of nitrogen. This indicates that inclusions have a stronger influence on the  $\gamma$  content. These results are consistent with the investigations of Sumita et al. [52].

### 3.3 Composition

The addition of oxygen and nitrogen to the shielding gas increased their respective contributions to the wall composition. In the Ar-O sample, the measured nitrogen content was higher than in the Ar sample, which is primarily due to the effect of oxygen on nitrogen preservation. This finding is consistent with the results of Du Toit and Pistorius [53], who reported in their study on A-TIG processes that oxygen in the shielding gas during WAAM prevented nitrogen loss in the samples. The chemical composition of the phases, including ferrite and austenite, was analyzed by EDS. Figure 13 shows a line scan starting in the ferrite phase, passing through the intragranular austenite and ending in the ferrite phase of the Ar sample. As the figure shows, the chromium and sulfur

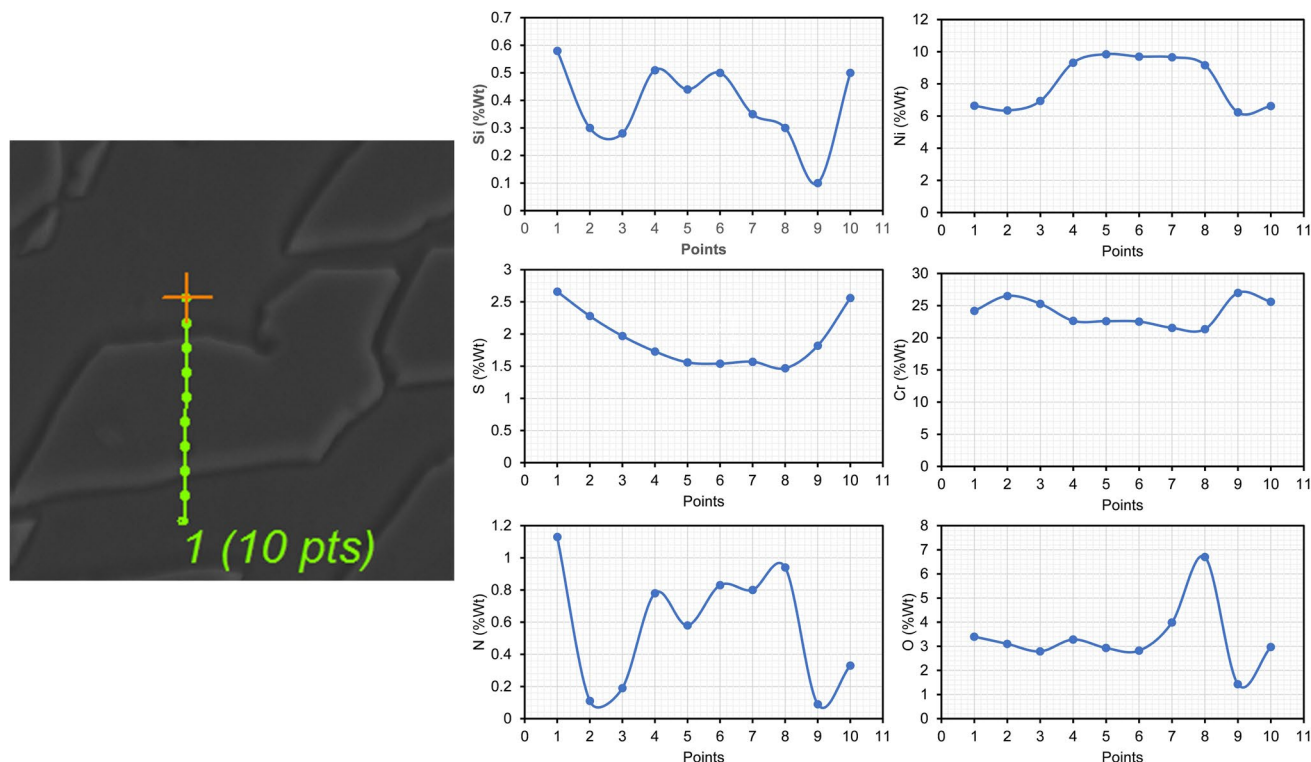


**Fig. 13** A line scan EDS elemental analysis of the Ar sample matrix, starting with the ferrite phase, passing through the austenite phase, and ending with the ferrite phase

contents are higher in the ferrite than in the austenite, while the austenite contains a higher concentration of nickel. A similar compositional trend was observed in the Ar–O and Ar–N samples, which is consistent with the reports of Sirohi et al. [54] and Zhou et al. [55].

### 3.4 Effect of Shielding Gas on Chromium Concentration

The chromium concentration in ten randomly selected ferrite and austenite phases in the as-deposited samples was determined by EDS, as shown in Fig. 14. The average concentration in each graph is represented by horizontal lines. The chromium concentration in the Ar sample was higher than in the other as-deposited samples in both the ferrite and austenite phases. The formation of chromium-rich inclusions or precipitates in the Ar–O and Ar–N samples could be responsible for the chromium depletion of ferrite and austenite, resulting in lower concentration values for the corresponding phases [56].

The total chromium content of the samples is calculated using the XRD results for the austenite and ferrite volume and the corresponding chromium concentration determined by EDS analysis according to the following equation:

$$Cr_T = V_A C_A + V_F C_F \quad (1)$$

where  $Cr_T$  is the total chromium concentration in the matrix of the samples and  $V_A$  and  $V_F$  are the austenite and ferrite fractions respectively and  $C_A$  and  $C_F$  are their Cr concentrations (in wt%) respectively.

The amount of chromium in the form of chromium-rich inclusions or precipitates can then be calculated using the following equations:

$$Cr_p(Ar - O) = Cr_T(Ar) - Cr_T(Ar - O) \quad (2)$$

$$Cr_p(Ar - N) = Cr_T(Ar) - Cr_T(Ar - N) \quad (3)$$

where  $Cr_p(Ar-O)$  and  $Cr_p(Ar-N)$  represent the total chromium concentrations in the form of precipitates, while  $Cr_T(Ar)$ ,  $Cr_T(Ar-O)$  and  $Cr_T(Ar-N)$  denote the total chromium concentrations in the matrix of the Ar, Ar–O, and Ar–N samples, respectively.

Using Eqs. (1–3),  $Cr_p(Ar-O)$  and  $Cr_p(Ar-N)$  were determined to be 1 and 1.1%, respectively. This means that 1% and 1.1% chromium is present as precipitates in the Ar–O and Ar–N samples respectively. In view of the large volume of inclusions in the Ar–O sample, it can be assumed that 1% chromium is contained in these inclusions. However, in the Ar–N sample, the volume of inclusions is significantly lower than in the Ar–O sample (0.24% for Ar–N and 1.5% for Ar–O). It appears that other precipitates may be present in the matrix in addition to the observed inclusions. Phase analysis of the XRD patterns of the Ar–N sample suggests that  $Cr_2N$  is a likely candidate for a small peak observed at about  $42.5^\circ 2\theta$ . The calculations for the Cr concentration in the Ar–N sample support this assumption. However, no  $Cr_2N$  precipitates were detected by electron microscopy, possibly due to their nanoscale size. Further characterization would require higher magnification electron microscopy.

### 3.5 EBSD Analysis

Figure 15a–f show the inverse pole figures (IPFs) maps, which were determined separately for the ferrite and austenite phases. The orientation intensity of these phases is shown in Fig. 16a–f, corresponding to the directions  $[001] \parallel BD$  and  $[010] \parallel TD$ . Regardless of the shielding gas used,

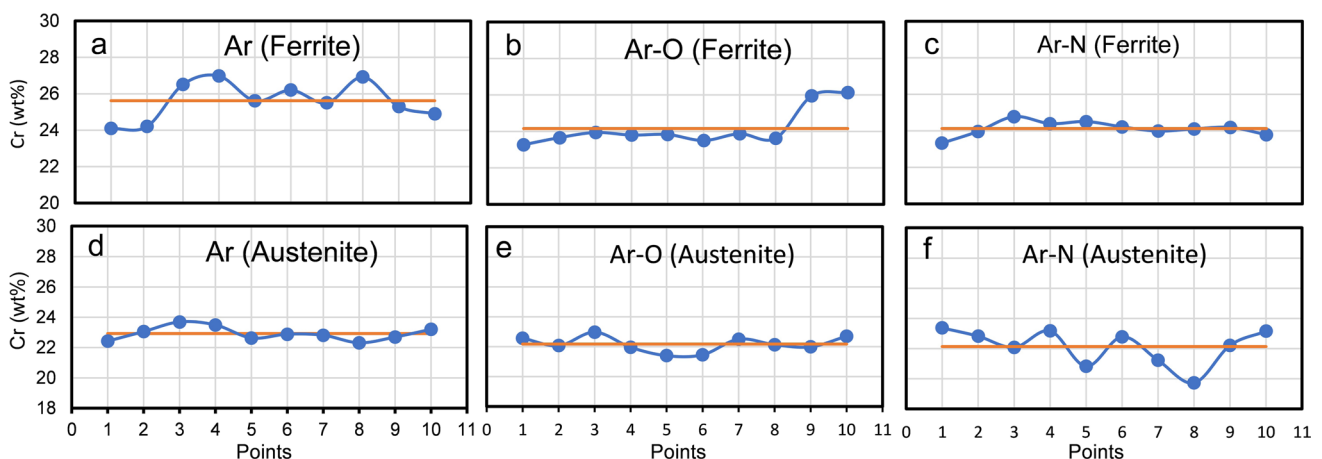


**Fig. 14** Chromium concentration (in wt%) taken from 10 various points for ferrite in **a** Ar, **b** Ar–O, and **c** Ar–N, and for austenite in **d** Ar, **e** Ar–O, and **f** Ar–N samples respectively

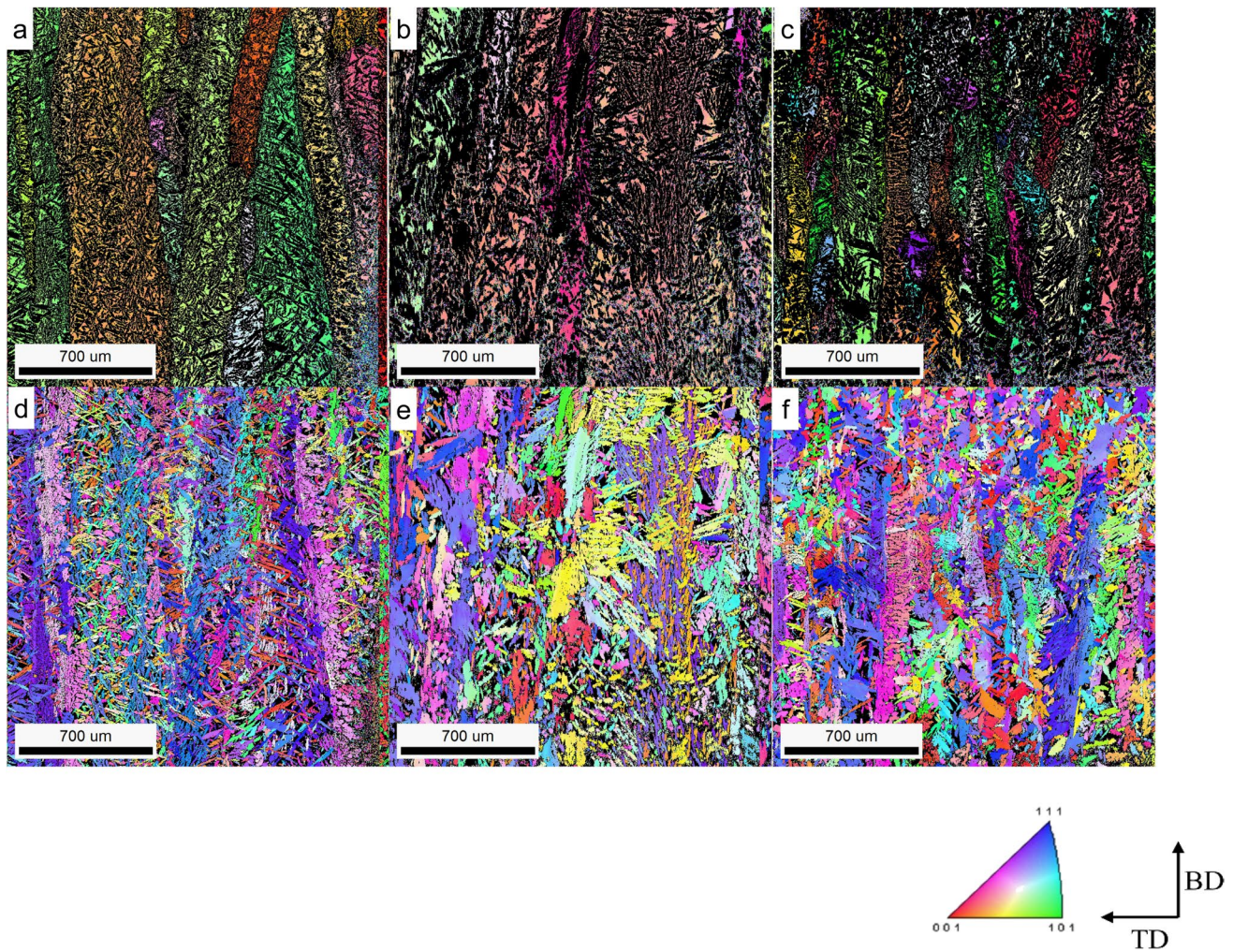


**Fig. 15** EBSD inverse pole figure (IPF) maps of ferrite in **a** Ar, **b** Ar–O, and **c** Ar–N and austenite in **d** Ar, **e** Ar–O, and **f** Ar–N samples

all three samples exhibited a pronounced texture in the  $[001]$   $\parallel$  BD direction for both the ferrite and austenite phases in the as-deposited state. The intensity of the anisotropy in the BD direction is significantly higher than in the TD direction, which is primarily due to the greater heat transfer in the BD direction. In particular, the intensity of this texture is significantly higher in the initial solidification phase (ferrite) than in the product of phase transformation in the solid state (austenite). In addition, the intensity of texture is more pronounced in the Ar sample compared to the Ar–O and Ar–N samples, with the Ar–O sample exhibiting the lowest anisotropy for both the ferrite and austenite phases (Fig. 17).

The IPFs results of the Ar–O sample indicate that the ferrite preferred orientation significantly influences the subsequent texture of the austenite. During the heating and cooling cycles, the grains tend to extend in the build-up direction (opposite to the direction with the highest heat transfer). However, the presence of nitrogen and inclusions in the Ar–N sample, as well as the presence of oxygen-rich

inclusions that remain stable at high temperatures in the Ar–O sample, hinder ferrite growth and reduce the texture intensity for both the ferrite and austenite phases. Nitrogen plays an important role as a strong austenite stabilizer in preventing the growth of ferrite grains [24]. In addition, undissolved austenite phase particles and stable oxides at high temperatures also limit the boundaries of the ferrite grains and can serve as nucleation sites for the formation of new orientations, leading to a random distribution of texture in comparison.

### 3.6 Mechanical Properties

#### 3.6.1 Microhardness

Figure 18 shows images of the hardness mapping carried out on 14 mm by 65 mm sections of the Ar, Ar–O and Ar–N samples. The color-coded hardness values show that the Ar–N sample has a significantly higher hardness

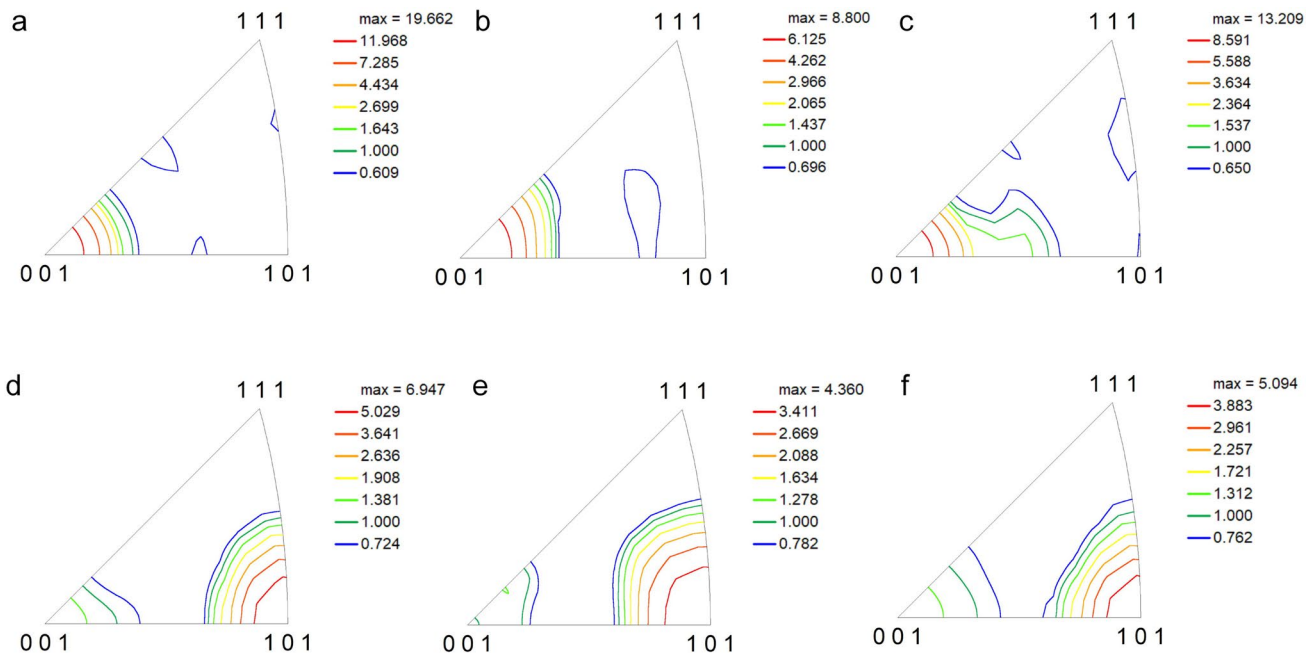


**Fig. 16** [001] IPF for ferrite in **a** Ar, **b** Ar–O, and **c** Ar–N and austenite in **d** Ar, **e** Ar–O, and **f** Ar–N samples ([001]  $\parallel$  BD)

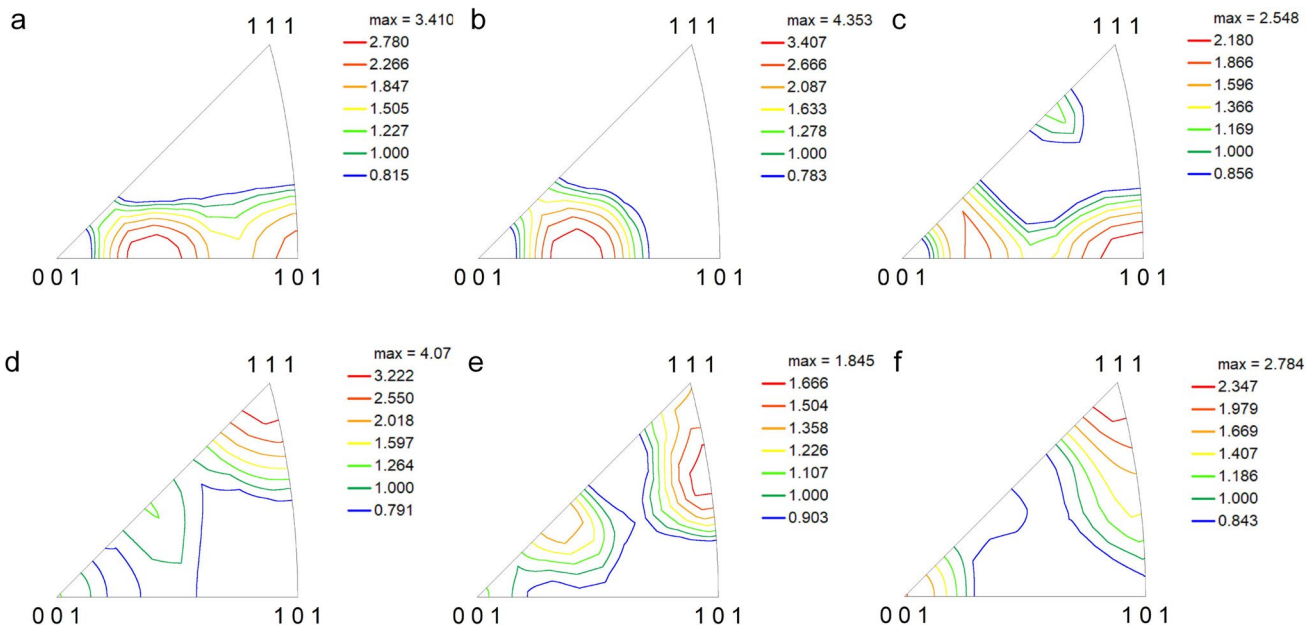


**Fig. 17** [010] IPF for ferrite in **a** Ar, **b** Ar–O, and **c** Ar–N and austenite in **d** Ar, **e** Ar–O, and **f** Ar–N samples ([010]  $\parallel$  TD)

compared to the other two samples. This increased hardness can be attributed to the strengthening effect of nitrogen on the austenite phase, as reported by Başığit et al. [57] on DSS welding. This observation is also confirmed by Martikainen [24], who reported a similar effect when the nitrogen content in an argon-based shielding gas was increased when welding 304 SS. Conversely, the Ar–O

sample exhibits the lowest hardness, which is due to the higher austenite content, as determined by XRD measurements and optical microscopy observations. In all three samples, a significant increase in hardness can be observed in the upper layers. This phenomenon can be attributed to the higher cooling rate in these layers, which leads to a lower austenite content.

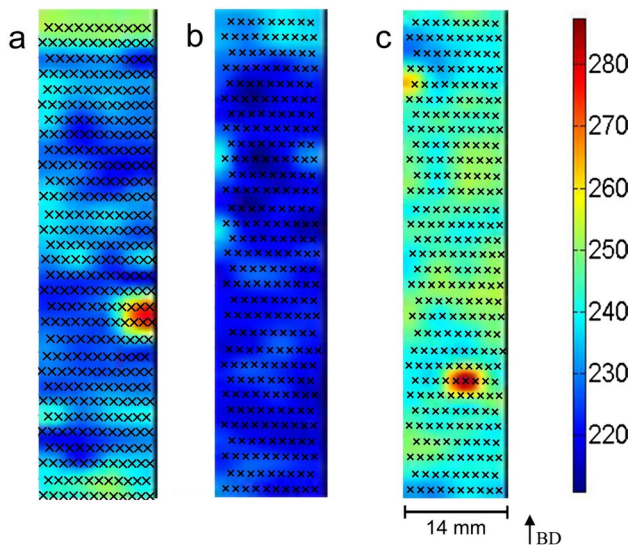


**Fig. 18** Hardness mapping images of samples produced using **a** Ar, **b** Ar–O and **c** Ar–N shielding gases. Building direction (BD) is also shown

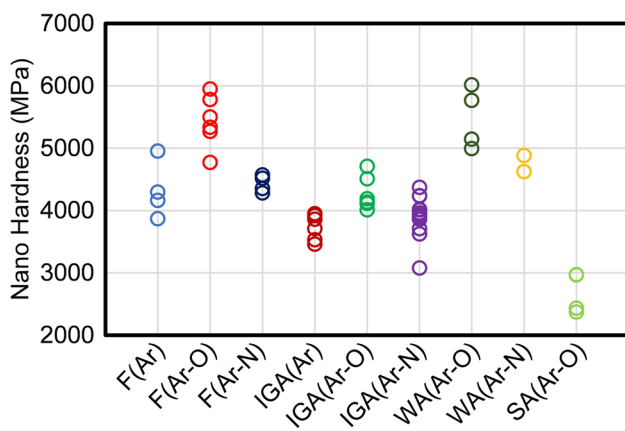


**Fig. 19** Nanoindentation results of the ferrite and austenite phases in Ar, Ar–O and Ar–N samples

Figure 19 shows the nano-hardness of ferrite and various austenite morphologies in Ar, Ar–O and Ar–N samples. The corresponding indentations with the hardness values are shown in the microscopic images in Fig. 20a–c for Ar, Ar–O and Ar–N samples respectively.

Ferrite is harder than austenite in all samples, which is consistent with the results of Gaderlab et al. on magnetic force microscopy studies on DSS [58]. Among the austenite morphologies, WA has the highest hardness. This was already reported by Jebaraj et al. in their studies on the weldability of DSS [59]. Nowacki and Łukojc [60] reported that the hardness of SA is influenced by the change in its chemical composition. The Cr content of SA is in the range of 11.52–14.21% according to several studies listed in reference

[59]. Presumably, the low hardness observed for SE is due to the relatively low Cr content compared to the other austenite morphologies.

### 3.6.2 Tensile Tests

Tensile tests were carried out on prepared samples of walls produced under three different shielding gases in both the longitudinal and vertical directions. The stress–strain curves for Ar, Ar–O and Ar–N specimens are shown in Fig. 21 and summarised in Table 3.

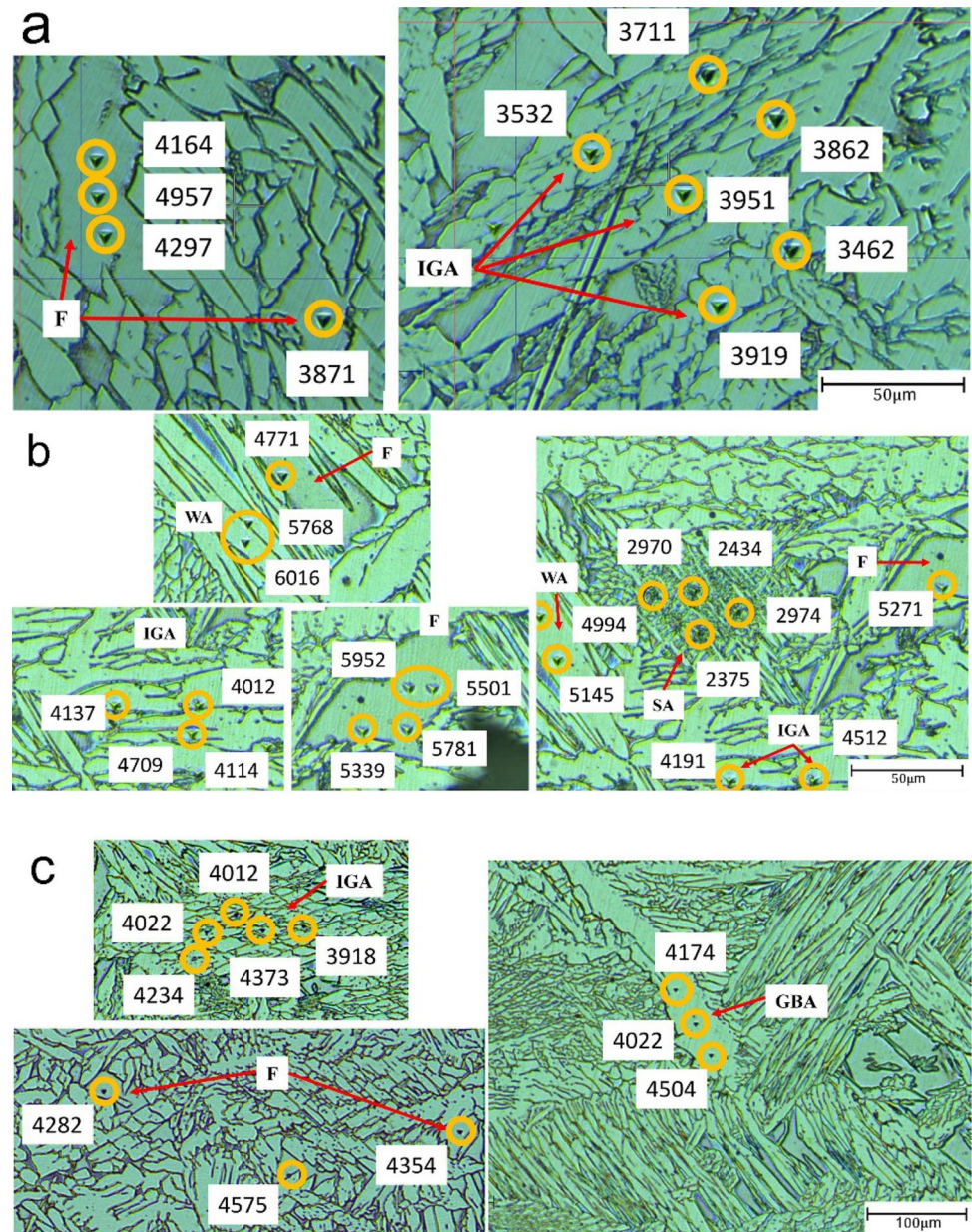
The specimen orientation has a considerable influence on the results of the tensile tests [61]. Regardless of the shielding gas composition, the values for yield strength and tensile strength are higher in the horizontal direction. This can be attributed to the higher grain boundary density in the horizontal direction [62]. The grain boundary strength at room temperature is higher than grain interior strength [63, 64]. Ar sample displays a good ductility despite its lower strength as shown by the stress–strain curves. The Ar–N specimen exhibits the highest yield and tensile strength values, especially in the vertical direction. This is due to the strengthening effect of nitrogen on the austenite phase. The higher nano-hardness values of the austenite in the Ar–N sample and the results of the hardness mapping confirm this finding. The graphs also show that rapid failure occurred in the Ar–O sample, possibly due to the high inclusion content. Ductile materials generally fail due to the nucleation, growth and coarsening of microscopic voids that form on inclusions or other second phase precipitates [65]. In the Ar–O sample with a higher content of inclusions, this process was faster and the sample did not exhibit plastic deformation before failure like the Ar sample.

Table 4 shows the tensile strength of WAAM 2209 DSS reported by various researchers. The strength of the Ar–N specimen in the current study exceeds the reported values.

### 3.7 Fractography

The fracture surfaces of the tensile specimens were examined using FESEM. The microscopic images are shown in Fig. 22 for the Ar, Ar–O and Ar–N specimens at different magnifications. As the figures show, all specimens failed by dimple rupture. Dimple rupture is caused by the coalescence of microcracks. The main difference between the fracture surfaces is the number of nucleation sites for microcracks, which leads to different sizes and distributions of the dimples [69]. If there are only a few microcrack nucleation sites, the cracks tend to grow large before they coalesce. In contrast, if there are many nucleation sites for microcracks, the cracks tend to coalesce faster, resulting in a higher number of smaller dimples [70, 71].

**Fig. 20** Optical micrographs showing the positions of nanoindentations and their corresponding hardness values for the **a** Ar, **b** Ar–O and **c** Ar–N sample



As can be seen in Fig. 22, there are clear differences between the samples in terms of both the number and depth of the samples. The Ar and Ar–N specimens show fewer dimples (Fig. 22b and h), indicating a lower presence of microcrack nucleation sites. However, some dimples in these samples have a greater depth. In contrast, the Ar–O sample exhibits a higher number of dimples with less depth (Fig. 22d), which is primarily due to the increased number of microcrack nucleation sites. In addition, significant differences in the degree of plastic deformation prior to failure were observed between the Ar and Ar–N specimens (Fig. 22a and g). It is noteworthy

that the Ar specimen undergoes greater plastic deformation compared to the Ar–N specimen. This observation is consistent with the results of the tensile tests (Fig. 22b).

Closer examination with higher magnification reveals the presence of inclusions within the dimples (Fig. 22e, c, f, i). The Ar–O sample in particular showed a considerable number of inclusions (Fig. 22f). Subsequent analysis revealed that these inclusions were complex oxides consisting of Si, Mn, Cr and Fe. The results of the EDS analysis of selected inclusions are shown in Fig. 22j and correspond to the inclusions marked with numbers.



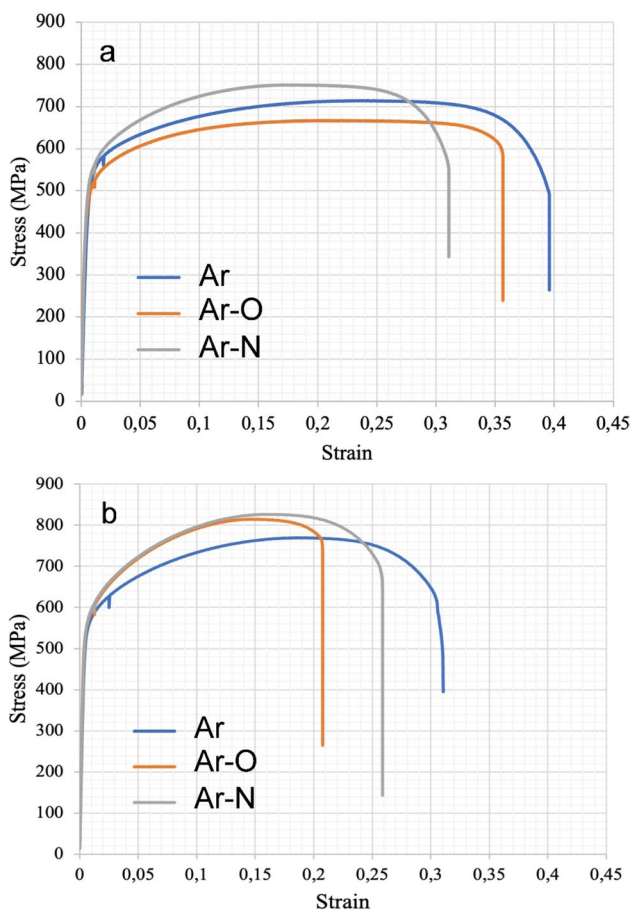


**Fig. 21** Stress–strain curves from tensile testing for Ar, Ar–O, and Ar–N samples fabricated in both **a** vertical and **b** horizontal directions

**Table 3** Yield strength (YS) and ultimate tensile strength (UTS) of Ar, Ar–O and Ar–N samples prepared in vertical and horizontal directions

Sample	YS vertical (MPa)	YS horizontal (MPa)	UTS vertical (MPa)	UTS horizontal (MPa)
Ar	488	530	714	769
Ar–O	459	538	667	814
Ar–N	490	539	751	826

**Table 4** Ultimate tensile strength (UTS) of WAAM 2209 DSS as reported in [66, 67] and [68] along with Ar–N sample from the current study

Shielding gas	UTS vertical (MPa)	References
Ar + 2.5%CO <sub>2</sub>	717	[66]
Ar flux-cored	682	[67]
Ar–N	795	[68]
Ar–N	826	Present study

## 4 Conclusions

In this study, the effects of shielding gas composition on the microstructural and mechanical properties of wire arc additive manufactured (WAAM) duplex stainless steel (DSS) using three different shielding gases, namely Ar, Ar + 2 wt%O<sub>2</sub> (Ar–O) and Ar + 2 wt%N<sub>2</sub> (Ar–N), were investigated. The main results are as follows:

- The inclusion content was determined to be 0.06, 1.5 and 0.24 (vol%) for the Ar, Ar–O and Ar–N samples, respectively.
- The greatest deviation from the typical 1:1 austenite to ferrite ratio was found in the Ar–O sample measuring a ratio of 0.85:0.15.
- Intragranular austenite was found to be the dominant morphology in the Ar–O sample. Secondary austenite morphology was also detected in several regions of the Ar–O sample, with a lower occurrence in the Ar–N sample.
- The Ar–O sample exhibited the lowest anisotropy among the samples.
- The hardness was measured at 250 HV and the tensile strength was measured at 826 MPa in the horizontal direction in the Ar–N sample, which was the highest of all samples.
- All samples exhibited dimple fracture, although there were differences in the number and depth of dimples. Complex oxides rich in Si, Mn, Cr, and Fe were detected on the fracture surfaces of the Ar–O and Ar–N samples.

This study underlines the crucial role of the selection of suitable shielding gases for the WAAM of duplex stainless steel. While oxygen-containing shielding gases are commonly used in conventional welding of 2209 DSS, this study shows that WAAM requires a different approach due to the formation of oxide inclusions, which have a negative effect on mechanical properties. Nitrogen-containing shielding gases, on the other hand, have advantages in terms of strength and hardness. For WAAM applications where a balance between strength and ductility is important, argon proves to be the preferred shielding gas. Future research could focus on optimizing WAAM parameters, such as heat input, to adjust the austenite to ferrite ratio while fine-tuning the oxygen content in the shielding gas to achieve better mechanical properties of the manufactured components.

**Acknowledgements** The authors would like to express their gratitude to the METU welding technology and nondestructive testing research/application center for their invaluable support in conducting this research.

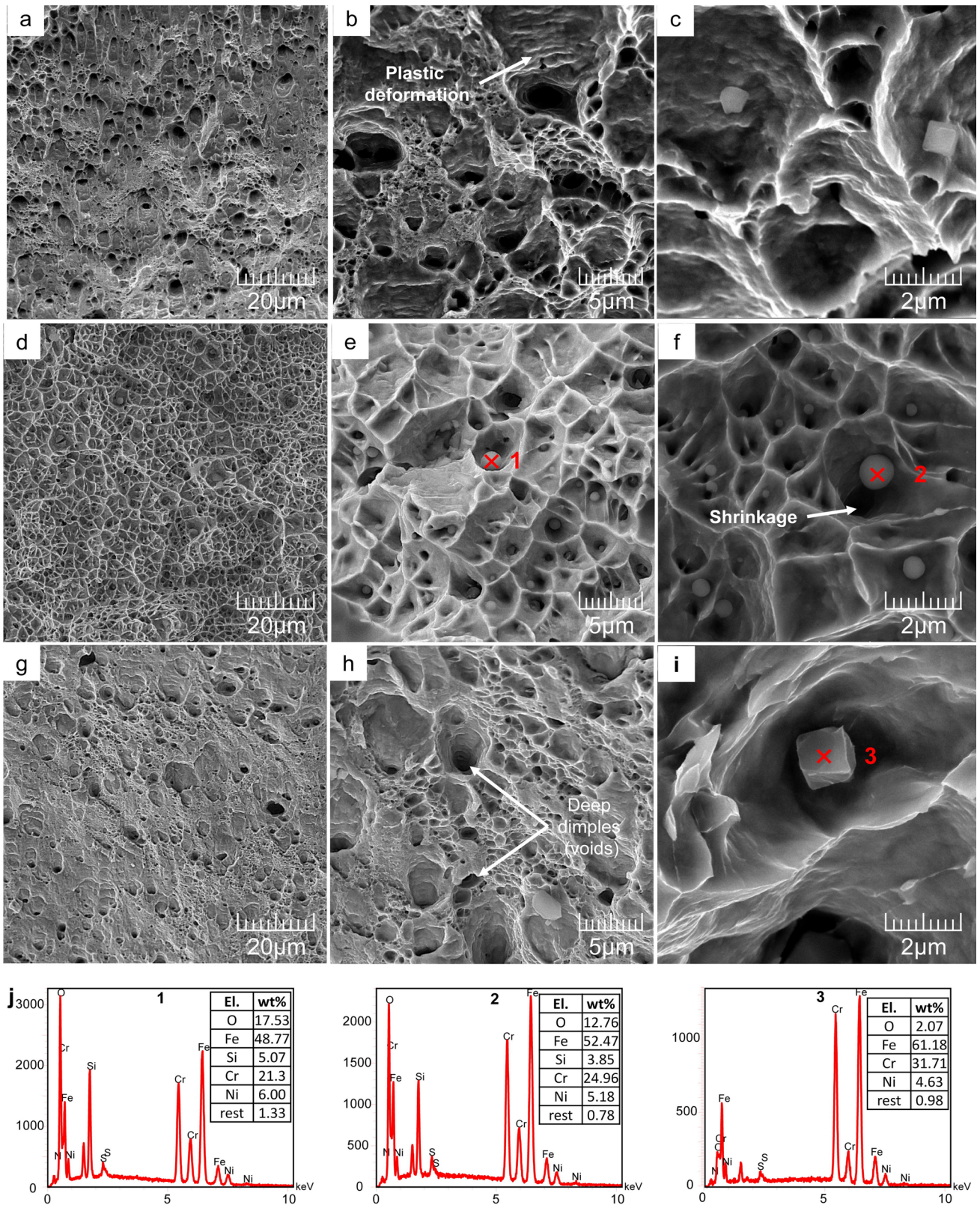


**Fig. 22** Fracture surface of tensile samples for **a–c** Ar, **d–f** Ar–O, **g–i** Ar–N samples and **j** EDS analysis of inclusions shown with corresponding numbers

## Declarations

**Conflict of interest** The authors have no competing interests to declare that are relevant to the content of this article.

## References

- J. Charles, P. Chemelle, The history of duplex developments, nowadays DSS properties and duplex market future trends, in *Duplex Stainless Steel: Proceedings of the 8th International Conference & Exhibition*, Beaune, 13–15 October 2010 (EDP Sciences, Les Ulis, 2010)
- P. Gowthaman, S. Jeyakumar, B. Saravanan, *Mater. Today Proc.* **26**, 1423 (2020). <https://doi.org/10.1016/j.matpr.2020.02.295>
- O. Steels, Practical guidelines for the fabrication of duplex stainless steels (International Molybdenum Association (IMO), London, 2014), [http://www.edelstahl.de/fileadmin/user\\_upload/ess\\_duplex\\_steel.pdf](http://www.edelstahl.de/fileadmin/user_upload/ess_duplex_steel.pdf)
- T. DebRoy, H. Wei, J. Zuback, T. Mukherjee, J. Elmer, J. Milewski, A.M. Beese, A.D. Wilson-Heid, A. De, W. Zhang, *Prog. Mater. Sci.* **92**, 112 (2018). <https://doi.org/10.1016/j.pmatsci.2017.10.001>
- A. Bandyopadhyay, K.D. Traxel, *Addit. Manuf.* **22**, 758 (2018). <https://doi.org/10.1016/j.addma.2018.06.024>
- V. Monfared, S. Ramakrishna, N. Nasajpour-Esfahani, D. Toghraie, M. Hekmatifar, S. Rahmati, *Met. Mater. Int.* **29**, 3442 (2023). <https://doi.org/10.1007/s12540-023-01467-x>
- N. Singh, H. Siddiqui, B.S.R. Koyalada, A. Mandal, V. Chauhan, S. Natarajan, S. Kumar, M. Goswami, S. Kumar, *Met. Mater. Int.* **29**, 2119 (2023). <https://doi.org/10.1007/s12540-022-01380-9>
- J. Liang, S. Yang, Y. Liu, X. Yin, S. Chen, C. Liu, *Met. Mater. Int.* **29**, 2052 (2023). <https://doi.org/10.1007/s12540-022-01360-z>
- B. Parvaresh, H. Aliyari, R. Miresmaeili, M. Dehghan, M. Mohammadi, *Met. Mater. Int.* **29**, 3103 (2023). <https://doi.org/10.1007/s12540-023-01444-4>
- Y. Xiong, D. Wen, Z. Zheng, C. Sun, J. Xie, J. Li, *Met. Mater. Int.* **29**, 3009 (2023). <https://doi.org/10.1007/s12540-023-01428-4>
- S.W. Williams, F. Martina, A.C. Addison, J. Ding, G. Pardal, P. Colegrove, *Mater. Sci. Technol.* **32**, 641 (2016). <https://doi.org/10.1179/1743284715Y.0000000073>
- A. Zadi-Maad, R. Rohib, A. Irawan, *IOP Conf. Ser.: Mater. Sci. Eng.* **285**, 012028 (2018). <https://doi.org/10.1088/1757-899X/285/1/012028>
- S. Singamneni, L. Yifan, A. Hewitt, R. Chalk, W. Thomas, D. Jordison, *J. Aeronaut. Aerosp. Eng.* **8**, 214 (2019). <https://doi.org/10.35248/2168-9792.19.8.215>
- M. Barath Kumar, M. Manikandan, *Met. Mater. Int.* **28**, 54 (2022). <https://doi.org/10.1007/s12540-021-01015-5>
- S. Srivastava, R.K. Garg, V.S. Sharma, A. Sachdeva, *Arch. Comput. Methods Eng.* **28**, 3491 (2021). <https://doi.org/10.1007/s11831-020-09511-4>
- W. Jin, C. Zhang, S. Jin, Y. Tian, D. Wellmann, W. Liu, *Appl. Sci.* **10**, 1563 (2020). <https://doi.org/10.3390/app10051563>
- B. Varbai, K. Májlinger, *Metals* **9**, 762 (2019). <https://doi.org/10.3390/met9070762>
- Y. Zou, X. Zhou, *J. Mater. Eng. Perform.* **32**, 6995 (2023). <https://doi.org/10.1007/s11665-022-07594-7>
- Z. Zhang, Y. Han, X. Lu, T. Zhang, Y. Bai, Q. Ma, *Mater. Sci. Eng. A* **872**, 144936 (2023). <https://doi.org/10.1016/j.msea.2023.144936>
- F. Binesh, A. Bahrami, M. Hebel, D.K. Aidun, *J. Mater. Eng. Perform.* **30**, 2552 (2021). <https://doi.org/10.1007/s11665-021-05593-8>
- M.A. Valiente Bermejo, L. Karlsson, L.E. Svensson, K. Hurtig, H. Rasmuson, M. Frodigh, P. Bengtsson, *Weld. World* **59**, 239 (2015). <https://doi.org/10.1007/s40194-014-0199-7>
- T. Nakamura, K. Hiraoka, S. Zenitani, *Sci. Technol. Weld. Join.* **13**, 25 (2008). <https://doi.org/10.1179/174329307X249289>
- C. Matz, G. Wilhelm, *Weld. Int.* **26**, 335 (2012). <https://doi.org/10.1080/09507116.2011.581341>
- P. Kah, J. Martikainen, *Int. J. Adv. Manuf. Technol.* **64**, 1411 (2013). <https://doi.org/10.1007/s00170-012-4111-6>
- Z. Liu, C.-L. Fan, Z. Ming, C. Chen, A. Liu, C.-L. Yang, S.-B. Lin, L.-P. Wang, *Def. Technol.* **17**, 923 (2021). <https://doi.org/10.1016/j.dt.2020.05.021>
- C. Li, H. Xue, X. Zhang, Y. Peng, K. Wang, *J. Mater. Eng. Perform.* (2023). <https://doi.org/10.1007/s11665-023-08770-z>
- Y. Zou, R. Ueji, H. Fujii, *Mater. Charact.* **91**, 42 (2014). <https://doi.org/10.1016/j.matchar.2014.02.006>
- D. Zhang, A. Liu, B. Yin, P. Wen, *J. Manuf. Process.* **73**, 496 (2022). <https://doi.org/10.1016/j.jmapro.2021.11.036>
- S. Patra, A. Agrawal, A. Mandal, A. Podder, *Trans. Indian Inst. Met.* **74**, 1089 (2021). <https://doi.org/10.1007/s12666-021-02278-7>
- E.G. Betini, M.P. Gomes, C.S. Mucsi, M.T. Orlando, T.D. Luz, M.N. Avettand-Fènoël, J.L. Rossi, *Mater. Res.* **22**, e20190247 (2019). <https://doi.org/10.1590/1980-5373-MR-2019-0247>
- A. Rokanopoulou, P. Skarvelis, G. Papadimitriou, *Weld. World* **63**, 3 (2019). <https://doi.org/10.1007/s40194-018-0660-0>
- Y. Zhang, S. Cheng, S. Wu, F. Cheng, *J. Mater. Process. Technol.* **277**, 116471 (2020). <https://doi.org/10.1016/j.jmatprotec.2019.116471>
- R. Zhou, D.O. Northwood, C. Liu, *J. Mater. Res. Technol.* **9**, 2331 (2020). <https://doi.org/10.1016/j.jmrt.2019.12.064>
- B. Varbai, Y. Adonyi, R. Baumer, T. Pickle, J. Dobránszky, K. Májlinger, *Weld. J.* **98**, 78-s (2019). <https://doi.org/10.29391/2019.98.006>
- S. Hertzman, J. Charles, *Rev. Metall.* **108**, 413 (2011). <https://doi.org/10.1051/metal/2011071>
- A.R. Pimenta, M.G. Diniz, G. Perez, I.G. Solórzano-Naranjo, *Soldag. Insp.* **25**, e2512 (2020). <https://doi.org/10.1590/0104-9224/SI25.12>
- Z. Zhang, H. Jing, L. Xu, Y. Han, L. Zhao, C. Zhou, *Appl. Surf. Sci.* **404**, 110 (2017). <https://doi.org/10.1016/j.apsusc.2017.01.252>
- V.A. Hosseini, M. Högström, K. Hurtig, M.A. Valiente Bermejo, L.-E. Stridh, L. Karlsson, *Weld. World* **63**, 975 (2019). <https://doi.org/10.1007/s40194-019-00735-y>
- E. Cederberg, V.A. Hosseini, C. Kumara, L. Karlsson, *Addit. Manuf.* **34**, 101269 (2020). <https://doi.org/10.1016/j.addma.2020.101269>
- M. Yoozbashi, S. Yazdani, *Mater. Chem. Phys.* **160**, 148 (2015). <https://doi.org/10.1016/j.matchemphys.2015.03.071>
- X. Xu, J. Ding, S. Ganguly, C. Diao, S. Williams, *J. Mater. Process. Technol.* **252**, 739 (2018). <https://doi.org/10.1016/j.jmatprotec.2017.10.030>
- W. Qiang, K. Wang, *J. Mater. Process. Technol.* **250**, 169 (2017). <https://doi.org/10.1016/j.jmatprotec.2017.07.021>
- Z. Liu, C.-L. Fan, C.-L. Yang, Z. Ming, S.-B. Lin, L.-P. Wang, *Def. Technol.* **27**, 138 (2023). <https://doi.org/10.1016/j.dt.2022.10.010>
- D. Yang, G. Wang, G. Zhang, *J. Mater. Process. Technol.* **244**, 215 (2017). <https://doi.org/10.1016/j.jmatprotec.2017.01.024>
- J. Verma, R.V. Taiwade, *J. Manuf. Process.* **25**, 134 (2017). <https://doi.org/10.1016/j.jmapro.2016.11.003>
- Q. Wang, G. Gu, C. Jia, K. Li, C. Wu, *J. Mater. Res. Technol.* **22**, 355 (2023). <https://doi.org/10.1016/j.jmrt.2022.11.107>
- A.J. Ramirez, J.C. Lippold, S.D. Brandi, *Metall. Mater. Trans. A* **34**, 1575 (2003). <https://doi.org/10.1007/s11661-003-0304-9>

48. S.H. Lee, *Metals* **10**, 278 (2020). <https://doi.org/10.3390/met10020278>
49. F. Montevercchi, G. Venturini, N. Grossi, A. Scippa, G. Campatelli, *Manuf. Lett.* **17**, 14 (2018). <https://doi.org/10.1016/j.mfglet.2018.06.004>
50. J. Fu, Z. Rao, Y. Zhao, J. Zou, X. Liu, Y. Pan, *Materials* **15**, 8741 (2022). <https://doi.org/10.3390/ma15248741>
51. D.A. Porter, K.E. Easterling, M.Y. Sherif, *Phase Transformations in Metals and Alloys* (CRC Press, Boca Raton, 2021)
52. M. Sumita, T. Hanawa, S. Teoh, *Mater. Sci. Eng. C* **24**, 753 (2004). <https://doi.org/10.1016/j.msec.2004.08.030>
53. M. Du Toit, P.C. Pistorius, *Weld. World* **53**, 38 (2009). <https://doi.org/10.1007/BF03266690>
54. S. Sirohi, C. Pandey, A. Goyal, *Mater. Today Proc.* **50**, 1367 (2022). <https://doi.org/10.1016/j.matpr.2021.08.280>
55. J. Zhou, J. Zhang, M. Liu, Z. Ma, Y. Yang, Z. Xu, C. Song, *Steel Res. Int.* **93**, 2200422 (2022). <https://doi.org/10.1002/srin.202200422>
56. D. Wen, B. Jiang, Z. Huang, F. Kong, X. Jiang, A. Wang, G. Liu, B. Wang, *J. Alloys Compd.* **954**, 170216 (2023). <https://doi.org/10.1016/j.jallcom.2023.170216>
57. A.B. Başıyigit, A. Kurt, *Metals* **8**, 226 (2018). <https://doi.org/10.3390/met8040226>
58. K.R. Gadelrab, G. Li, M. Chiesa, T. Souier, *J. Mater. Res.* **27**, 1573 (2012). <https://doi.org/10.1557/jmr.2012.99>
59. A. Vinoth Jebaraj, L. Ajaykumar, C.R. Deepak, K.V.V. Aditya, *J. Adv. Res.* **8**, 183 (2017). <https://doi.org/10.1016/j.jare.2017.01.002>
60. J. Nowacki, A. Łukojć, *J. Mater. Process. Technol.* **164–165**, 1074 (2005). <https://doi.org/10.1016/j.jmatprotec.2005.02.243>
61. H. Chae, E.W. Huang, J. Jain, D.-H. Lee, S. Harjo, T. Kawasaki, S.Y. Lee, *Met. Mater. Int.* (2023). <https://doi.org/10.1007/s12540-023-01575-8>
62. C. Gao, X. Chen, C. Su, X. Chen, *Vacuum* **168**, 108818 (2019). <https://doi.org/10.1016/j.vacuum.2019.108818>
63. G.E. Dieter, D. Bacon, *Mechanical Metallurgy* (McGraw-Hill Book Company (UK) Limited, London, 1988)
64. A.H. Chokshi, *Adv. Eng. Mater.* **22**, 1900748 (2020). <https://doi.org/10.1002/adem.201900748>
65. T.L. Anderson, *Fracture Mechanics: Fundamentals and Applications* (CRC Press, Boca Raton, 2017)
66. G. Posch, K. Chladil, H. Chladil, *Weld. World* **61**, 873 (2017). <https://doi.org/10.1007/s40194-017-0474-5>
67. F. Hejripour, F. Binesh, M. Hebel, D.K. Aidun, *J. Mater. Process. Technol.* **272**, 58 (2019). <https://doi.org/10.1016/j.jmatprotec.2019.05.003>
68. Y. Zhang, F. Cheng, S. Wu, *J. Manuf. Process.* **69**, 204 (2021). <https://doi.org/10.1016/j.jmapro.2021.07.045>
69. B. Bagheri, M. Abbasi, M. Dadaei, *Metallogr. Microstruct. Anal.* **9**, 33 (2020). <https://doi.org/10.1007/s13632-019-00606-4>
70. J.L. González-Velázquez, *Fractography and Failure Analysis* (Springer, Cham, 2018)
71. B. Bagheri, A. Abdollahzadeh, A. Shamsipur, *Mater. Sci. Technol.* **39**, 1083 (2023). <https://doi.org/10.1080/02670836.2022.2159633>

**Publisher's Note** Springer Nature remains neutral with regard to jurisdictional claims in published maps and institutional affiliations.

Springer Nature or its licensor (e.g. a society or other partner) holds exclusive rights to this article under a publishing agreement with the author(s) or other rightsholder(s); author self-archiving of the accepted manuscript version of this article is solely governed by the terms of such publishing agreement and applicable law.